**Showcasing research from the key Laboratory for Colloid and Interface Chemistry, School of Chemistry and Chemical Engineering, Shandong University, Jinan, China, and Shanghai Synchrotron Radiation Facility, Shanghai Institute of Applied Physics, Chinese Academy of Sciences, Shanghai, China.**

Uniform 2 nm gold nanoparticles supported on iron oxides as active catalysts for CO oxidation reaction: structure–activity relationship

Active gold-iron oxide catalysts with uniform size of 2 nm for gold nanoparticles have been prepared by both deposition-precipitation and colloidal-deposition methods. Higher level of effectiveness of interaction formed through gold nanoparticles locally generated on the oxide support in DP, while hydroxylated surface favors the reactivity of externally introduced Au nanoparticles on Fe_OH support in CD.

ROYAL SOCIETY
OF CHEMISTRY
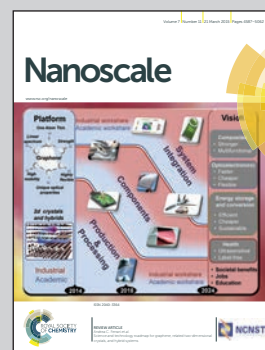
www.rsc.org/nanoscale

Uniform 2 nm gold nanoparticles supported on iron oxides as active catalysts for CO oxidation reaction: structure–activity relationship

Yu Guo,[a] Dong Gu,[b] Zhao Jin,[a] Pei-Pei Du,[c] Rui Si,*[c] Jing Tao,[d] Wen-Qian Xu,[e] Yu-Ying Huang,[c] Sanjaya Senanayake,[e] Qi-Sheng Song,[a] Chun-Jiang Jia*[a] and Ferdi Schüth[b]

Uniform Au nanoparticles (~2 nm) with narrow size-distribution (standard deviation: 0.5–0.6 nm) supported on both hydroxylated (Fe_OH) and dehydrated iron oxide (Fe_O) have been prepared by either deposition-precipitation (DP) or colloidal-deposition (CD) methods. Different structural and textural characterizations were applied to the dried, calcined and used gold-iron oxide samples. Transmission electron microscopy (TEM) and high-resolution TEM (HRTEM) showed high homogeneity in the supported Au nanoparticles. The *ex situ* and *in situ* X-ray absorption fine structure (XAFS) characterization monitored the electronic and short-range local structure of active gold species. The synchrotron-based *in situ* X-ray diffraction (XRD), together with the corresponding temperature-programmed reduction by hydrogen (H_2-TPR), indicated a structural evolution of the iron-oxide supports, correlating to their reducibility. An inverse order of catalytic activity between DP (Au/Fe_OH < Au/Fe_O) and CD (Au/Fe_OH > Au/Fe_O) was observed. Effective gold-support interaction results in a high activity for gold nanoparticles, locally generated by the sintering of dispersed Au atoms on the oxide support in the DP synthesis, while a hydroxylated surface favors the reactivity of externally introduced Au nanoparticles on Fe_OH support for the CD approach. This work reveals why differences in the synthetic protocol translate to differences in the catalytic performance of Au/FeO_x catalysts with very similar structural characteristics in CO oxidation.

1. Introduction

Low-temperature CO oxidation over supported nanosized gold catalysts has been one of the most extensively studied systems in heterogeneous catalysis.[1–3] However, this simple reaction, catalyzed by nanostructured gold, is still very difficult to understand in depth. It is known that various factors, including the size of gold nanoparticles,[1,4,5] the valence state of gold species (metallic Au^0 and ionic $Au^{\delta+}$),[6–8] the oxide support,[9–14] and the metal-support interaction,[15,16] can influence the catalytic performance of supported gold catalysts. However, previous

findings with respect to the origin of high activity of gold catalysts are rather controversial, and the debate over the reaction mechanism of low-temperature CO oxidation has continued for more than two decades because of the ultra sensitivity and complexity of the oxide-supported gold system. One of the origins of this debate lies in the interrelationship of the different factors mentioned above, which are very difficult to be distinguished from each other in gold catalysis.

Gold on iron-oxide (Au/FeO_x) is one of the most active catalysts for CO oxidation, and is also a typical system for the study of the chemistry of gold on oxide supports.[4,5,17] Regarding the widely studied coprecipitated (CP) Au/FeO_x catalysts that have wide size-distribution of gold particles (from sub-nanometer to more than 20 nm),[4] it has been discovered that as-dried samples are considerably more active for CO oxidation than those after sintering, indicating the negative effect of calcination on activity.[4,17] In fact, the calcination of gold-iron oxide catalysts usually results in simultaneous structural changes of both the gold and the oxide support, *i.e.*, small gold clusters (<1 nm) with dominant cationic components are transformed into purely metallic nanoparticles (>1 nm); in addition, the phase of the support changes from hydroxylated ferrihydrite to

[a] Key Laboratory for Colloid and Interface Chemistry, Key Laboratory of Special Aggregated Materials, School of Chemistry and Chemical Engineering, Shandong University, Jinan 250100, China. E-mail: jiacj@sdu.edu.cn
[b] Max-Planck Institut für Kohlenforschung, Kaiser-Wilhelm Platz 1, Mülheim an der Ruhr, D-45470, Germany
[c] Shanghai Synchrotron Radiation Facility, Shanghai Institute of Applied Physics, Chinese Academy of Sciences, Shanghai 201204, China. E-mail: sirui@sinap.ac.cn
[d] Condensed Matter Physics and Materials Science Department, Brookhaven National Laboratory, Upton, New York 11973, USA
[e] Chemistry Department, Brookhaven National Laboratory, Upton, New York 11973, USA
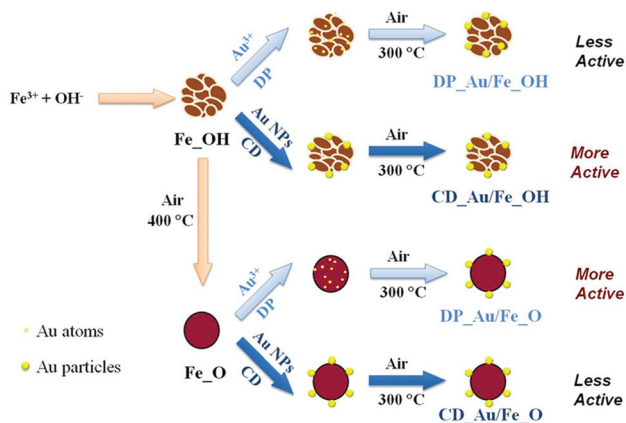
Scheme 1 Schematic demonstration of the formation pathways of the different Au/FeO$_x$ catalysts.

dehydrated hematite.[17] For this catalyst system, the accurate analysis of the origin of CO oxidation activity is a substantial challenge due to the combination between various structural and textural effects. Thus, the separate synthesis of gold nanoparticles with narrow size distribution and iron oxide supports with specific structure is crucial to rationally investigate the structure–activity relationship of Au/FeO$_x$ catalysts.

In this paper, we try to identify the support effect and the formation of gold nanostructure of Au/FeO$_x$ catalysts for CO oxidation using deposition-precipitation (DP)[18] or colloidal-deposition (CD)[13] syntheses for anchoring gold on hydroxylated (Fe_OH) or dehydrated iron oxide (Fe_O) supports (Scheme 1). Highly dispersed gold nanoparticles (~2 nm) with narrow size distribution (standard deviation: 0.5–0.6 nm) were obtained. The catalysts were studied by a combination of transmission electron microscopy (TEM) and high-resolution TEM (HRTEM), *ex situ* and *in situ* X-ray absorption fine structure (XAFS), and *in situ* X-ray diffraction (XRD) techniques. These unique samples allow us to distinguish the different factors (particle size, metal-support interaction, surface hydroxyl effect) governing the catalytic activity of gold-iron oxide catalyst. It is also demonstrated how important are the formation pathways (locally generated or externally introduced) of gold particles for the generation of active sites.

2. Experimental

2.1. Catalyst preparation

2.1.1 Preparation of iron oxide supports.[7] In a typical procedure, a 0.25 mol L^{-1} Na$_2$CO$_3$ aqueous solution was added drop-wise to 200 mL of 0.1 mol L^{-1} Fe(NO$_3$)$_3$ aqueous solution with stirring at 80 °C until pH = 8.2 was reached, and stirred for another 1 h. The precipitate was collected by filtration and washed with deionized (DI) water at 80 °C. This precipitate was dried at 120 °C in air for *ca.* 12 h to generate the hydrated iron oxide support (Fe_OH). The oxide support (Fe_O) was obtained *via* calcination of Fe_OH in air at 400 °C for 2 h.

2.1.2 Preparation of gold-iron oxide catalysts *via* colloidal deposition.[13] For colloidal deposition, poly(vinyl alcohol) (PVA, M_w 10 000 from Aldrich, 80% hydrolyzed) was used as the protecting agent. Typically, 0.675 mL of 0.5 wt% PVA solution (Au : PVA = 1.5 : 1 in weight) and 2 mL of 0.0125 mol L^{-1} HAuCl$_4$ solution were added into 50 mL of Millipore water (18.25 MΩ) at room temperature with vigorous stirring. After stirring for 10 min, a rapid injection of 1.3 mL of 0.1 mol L^{-1} NaBH$_4$ aqueous solution led to the formation of a dark orange–brown solution. 0.5 g Fe_OH or Fe_O was then immediately added to the colloidal gold solution with vigorous stirring, which was continued for 6 h until complete adsorption of the gold (1 wt%), as indicated by the decoloration of the solution. The solids were collected by filtration and washed with Millipore water to remove the dissolved impurities (Cl$^-$, *e.g.*). After drying the sample overnight at 60 °C in air, CD_Au/Fe_OH and CD_Au/Fe_O were obtained. All the abovementioned steps were carried out in the absence of light by covering all the containers with aluminum foil.

2.1.3 Preparation of gold-iron oxide catalysts *via* deposition precipitation. Typically, 0.5 g support powder (Fe_OH or Fe_O) was suspended in 23 mL Millipore water. 2 mL of 0.0125 mol L^{-1} HAuCl$_4$ aqueous solution was then added to the solution under stirring at *ca.* 60 °C. After 30 min, 25 mL of aqueous solution containing 0.5 g of urea was quickly added into the stock solution. Thereafter, the solution temperature was increased to 80 °C and vigorously stirred for 3 hours to allow the decomposition of urea, which resulted in a gradual increase in the pH value from 4.0 to 8.6. The solution was aged at room temperature for another 20 h. The as-obtained solids were collected by filtration, and then washed with Millipore water at 60 °C. After drying at 60 °C overnight in air, DP_Au/Fe_OH and DP_Au/Fe_O were obtained.

2.2. Characterization

The gold loadings of catalysts were determined by inductively coupled plasma atomic emission spectroscopy (ICP-AES) on an IRIS Intrepid II XSP instrument (Thermo Electron Corporation).

Transmission electron microscopy (TEM), high-resolution TEM (HRTEM) and the related high angle annular dark field-scanning TEM (HAADF-STEM) were conducted on a Philips Tecnai F20 instrument at 200 kV and a field emission TEM (JEOL 2100F) machine equipped with a 2k × 2k CCD camera at 200 kV. All the tested samples were ground in a mortar alone rather than suspended in ethanol before deposition on an ultra-thin carbon film-coated copper grid.

Temperature-programmed reduction by hydrogen (H$_2$-TPR) was carried out in a Builder PCSA-1000 instrument (Beijing, China) equipped with a thermal conductivity detector (TCD) to detect H$_2$ consumption. The sieved catalysts (20–40 mesh, 30 mg) were heated (5 °C min^{-1}) from room temperature to 400 °C in a 20% H$_2$/Ar (30 mL min^{-1}) gas mixture. Before the measurements were taken, the fresh samples were pretreated in pure O$_2$ at 300 °C for 30 min.

X-ray absorption fine structure (XAFS): Au L-III absorption edge (E_0 = 11 919 eV) XAFS spectra were collected *ex situ* at

BL14W1 beamline of the Shanghai Synchrotron Radiation Facility (SSRF) operated at 3.5 GeV under "top-up" mode with a current of 220 mA. The XAFS data were collected in fluorescence mode with a 32 element Ge Solid State Detector (SSD). The *in situ* experiments were conducted at the X18B beamline of the National Synchrotron Light Source (NSLS) at Brookhaven National Laboratory (BNL), operated at 2.8 GeV under "decay" mode with currents of 160–300 mA. The powder sample (~25 mg) was loaded into a Kapton tube (O.D. = 0.125 inch), which was attached to an *in situ* flow cell. Two small resistance heating wires were installed above and below the tube, and the temperature was monitored with a 0.5 mm chromel-alumel thermocouple that was placed inside the tube near the sample. The *in situ* CO oxidation reaction (1%CO/16% O_2/83%He, 20 mL min^{-1}) was carried out under a "steady-state" mode at room temperature (~25 °C). Each XAFS spectrum (*ca.* 15 min collection) was taken under fluorescence mode with a 4 element Vortex Silicon Drift Detector (SDD). The energy was calibrated for each scan with the first inflection point of the Au L-III-edge in Au metal foil. The X-ray absorption near edge spectroscopy (XANES) and extended X-ray absorption fine structure (EXAFS) data have been analyzed using the Athena and Artemis programs.

X-ray diffraction (XRD): the *ex situ* and *in situ* XRD experiments were carried out on X7B beamline (λ = 0.3196 Å) of NSLS at BNL. The powder sample (~2 mg) was loaded into a quartz tube (I.D. = 0.9 mm, O.D. = 1.0 mm) that was attached to the same flow cell as in the XAFS measurements. One small resistance heating wire was installed right below the tube, and the temperature was monitored with a 0.5 mm chromel-alumel thermocouple that was placed inside the tube, near the sample. The *in situ* H_2-TPR tests (5%H_2/Ar, 5 ml min^{-1}) were carried out using a temperature ramp between 25 and 400 °C (5 °C min^{-1}), and then maintained at 400 °C for 20 min. The fresh catalysts were pretreated in 5%O_2/He at 300 °C for 30 min before *in situ* measurements. Two-dimensional XRD patterns were collected with an image-plate detector (Perkin-Elmer), and the powder rings were integrated using the FIT2D code.

2.3. Catalytic test

CO oxidation activities of gold-iron oxide catalysts were measured in a plug flow reactor using 50 mg of sieved (20–40 mesh) catalyst in a gas mixture of 1 vol% CO, 20 vol% O_2, and 79 vol% N_2 (from AIR LIQUIDE, 99.997% purity), at a flow rate of 67 mL min^{-1}, corresponding to a space velocity of 80 000 mL h^{-1} g$_{cat}$$^{-1}$. Prior to the measurement, the catalysts were pretreated in air at 300 °C for 30 min for activation. After that, the reactor was cooled down to −50 °C under a flow of pure N_2 gas. The catalytic tests were carried out in the reactant atmosphere by ramping the catalyst temperature (5 °C min^{-1}) from −50 to 300 °C. The outlet gas compositions of CO and CO_2 were monitored online by a non-dispersive IR spectroscopy (ABB EL 3020). (CO conversion = CO $_{reaction}$/CO$_{input}$ = CO_2 $_{output}$/(CO_2 $_{output}$ + CO$_{output}$). A typical "steady-state" experiment (30 °C) was conducted in the same gas-mixture at 30 °C for more than 10 h.

3. Results and discussion

The ICP-AES results (Table 1) show that the experimental Au loading of all four catalysts are close to the target value of 1 wt%. The XRD data (Fig. 1) reveal that the Fe_OH supports in the catalysts are semi-amorphous (see pattern a/b), probably a mixture of several hydroxylated iron oxide phases, even after air-calcination at 300 °C. On the other hand, Fe_O obtained by the thermal dehydration of Fe_OH, is present as well-defined hematite (α-Fe_2O_3, JCPDS card#: 2-919) in both DP (pattern c) and CD (pattern d) samples, indicating the complete dehydration and crystallization during the 400 °C air-calcination. The TEM images (Fig. 2 and 3) allow the determination of the sizes of Fe_OH and Fe_O supports to ~5 and 10–30 nm, respectively. For the dried DP samples, no gold clusters/particles were found by HRTEM (Fig. 2a and 2b). This suggests that the gold atoms are well dispersed on the surfaces of iron-based supports before air-calcination. On the other hand, for the dried CD catalysts, ~2 nm Au nanoparticles on Fe_OH and Fe_O surfaces were clearly observed in TEM (Fig. 3a and 3b) due to features of the colloidal deposition preparation, *i.e.* well-crystallized small-size gold particles already formed before adding the iron-based supports.

In addition to the characterization by electron microscopy, we also carried out XAFS analysis to determine the coordi-

Table 1 Characterization of gold catalyst

Sample	Au^a (wt%)	Phase^b	D^c (nm)	S^d (m^2 g^{-1})
DP_Au/Fe_OH	0.92	Amorphous	2.2 ± 0.6	210
DP_Au/Fe_O	0.89	α-Fe_2O_3	2.0 ± 0.5	69
CD_Au/Fe_OH	0.98	Amorphous	2.0 ± 0.6	210
CD_Au/Fe_O	0.96	α-Fe_2O_3	2.1 ± 0.6	66

^{a} Determined by ICP-AES. ^{b} Identified from XRD patterns for calcined catalysts. ^{c} Mean Au particle sizes of calcined catalysts, which were calculated from >100 nanoparticles in HRTEM images. ^{d} BET surface areas for calcined catalysts.
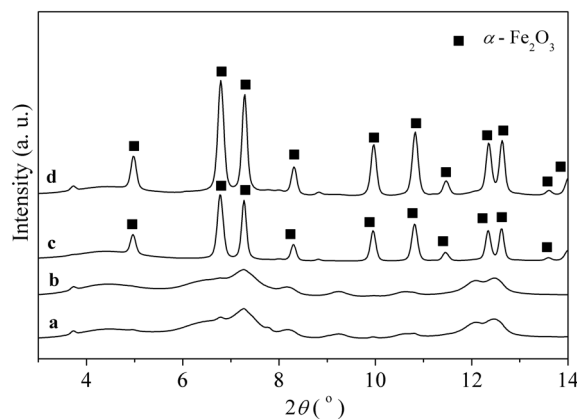

Fig. 1 XRD patterns of calcined Au/FeO$_x$ samples: (a) DP_Au/Fe_OH; (b) CD_Au/Fe_OH; (c) DP_Au/Fe_O; (d) CD_Au/Fe_O.
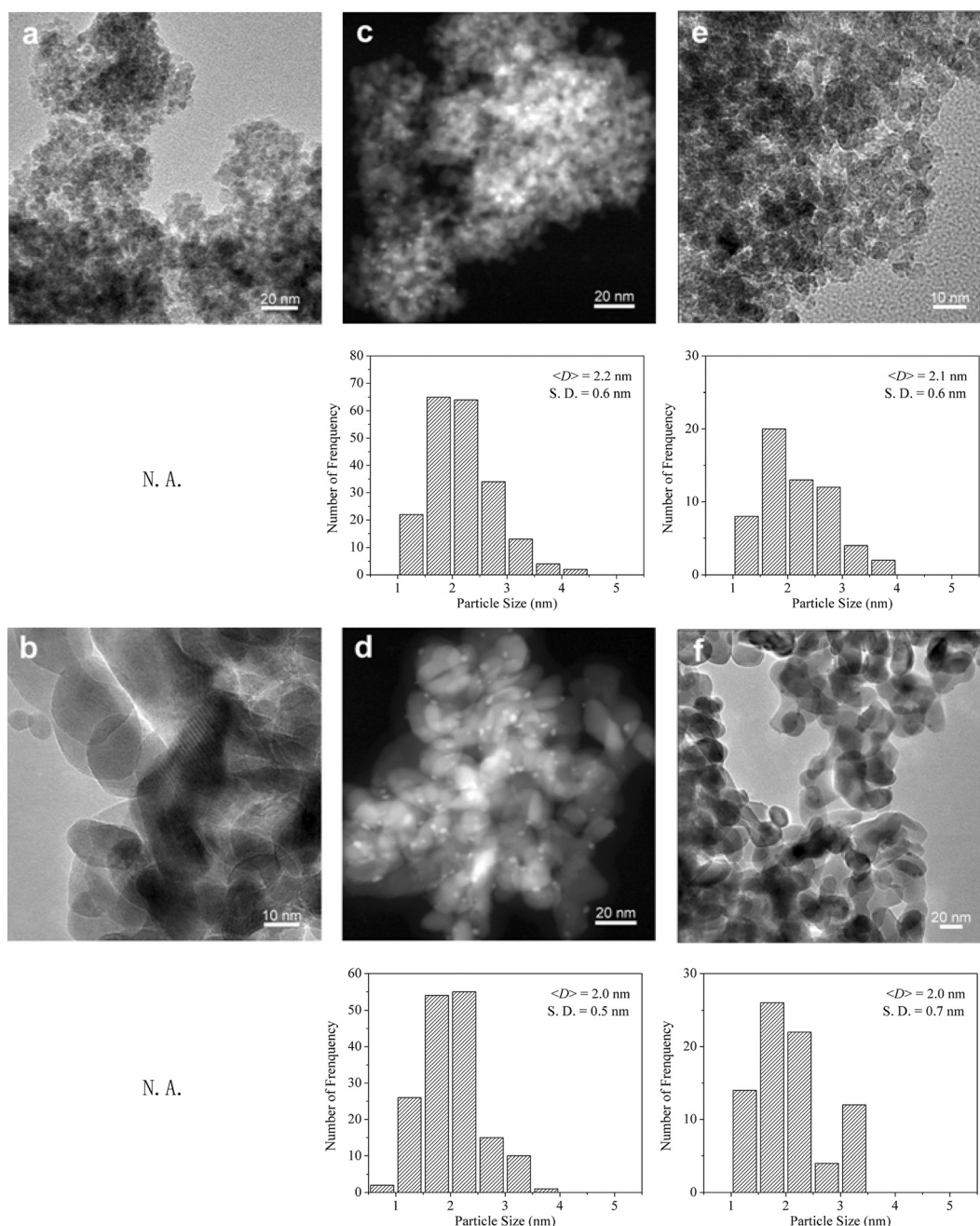
Fig. 2 TEM/HRTEM and HAADF-STEM images of (a) dried DP_Au/Fe_OH; (b) dried DP_Au/Fe_O; (c) calcined DP_Au/Fe_OH; (d) calcined DP_Au/Fe_O; (e) used DP_Au/Fe_OH; (f) used DP_Au/Fe_O. The size distribution of the gold particles is shown in the rows underneath the corresponding TEM images.

nation state of the gold species (Table 2 and Fig. 4). The X-ray absorption near edge structure (XANES) spectra reveal the ionic nature of Au species[19] in the dried DP catalysts (Fig. 4a and 4b), and the related extended XAFS (EXAFS) spectra (Fig. 4c and 4d) show the presence of a pure Au–O shell in the dried DP_Au/Fe_OH and DP_Au/Fe_O samples, with distances of the first coordination sphere of *ca.* 2.0 Å and coordination numbers (CN) of 2.5–2.9 by EXAFS fittings (Table 2), which are consistent with a previous report on fully oxidized Au$^{\delta+}$ species in gold-ceria catalysts.[20] For the CD samples, according to the

corresponding XANES (Fig. 5a) and EXAFS (Fig. 5b) results, gold species were in metallic form with a CN of 10–11 (Table 2), well consistent with the Au^0 nanoparticle nature.

Upon calcination, the well-dispersed atomic gold species in DP samples were transformed to uniform small (*ca.* 2 nm) nanoparticles, as seen in the HAADF-STEM images in Fig. 2c and 2d (also refer to Table 1). The XANES spectra display distinct metallic gold (Au^0) features for calcined DP_Au/Fe_OH and DP_Au/Fe_O catalysts (Fig. 4a and 4b), and the corresponding EXAFS fitting results confirm this because only
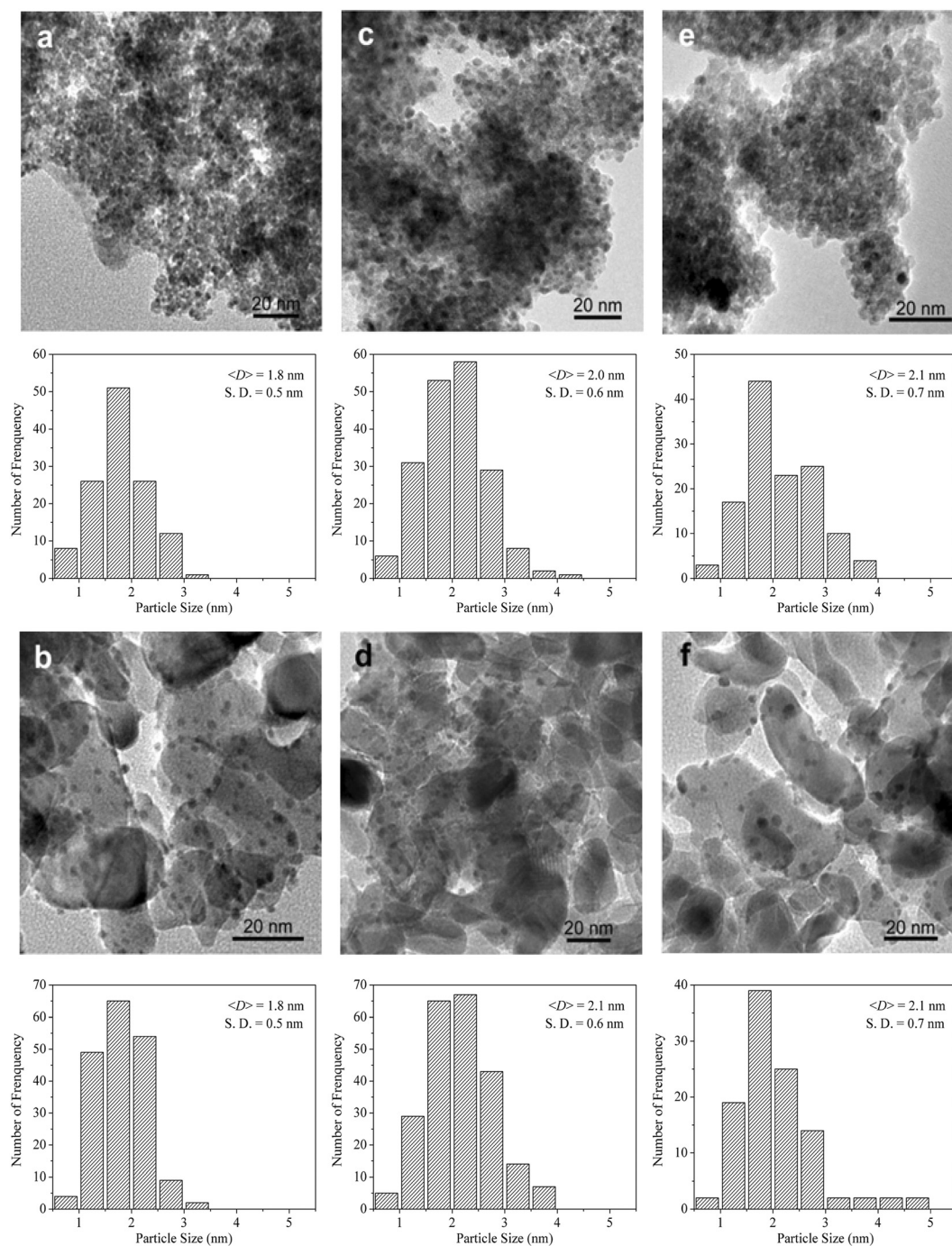
Fig. 3 TEM/HRTEM images of (a) dried CD_Au/Fe_OH; (b) dried CD_Au/Fe_O; (c) calcined CD_Au/Fe_OH; (d) calcined CD_Au/Fe_O; (e) used CD_Au/Fe_OH; (f) used CD_Au/Fe_O. The size distribution of the gold particles is shown in the rows underneath the corresponding TEM images.

Au–Au contributions (2.84 Å, CN = 10, refer to Table 2, Fig. 4c and 4d) are present, instead of the Au–O shell in the dried samples. The formation of gold nanoparticles after the 300 °C air-calcination demonstrates the relatively weaker interaction between Au atoms and the Fe_OH or Fe_O support in DP samples than that of the widely studied coprecipitated Au/FeO$_x$ catalysts, *i.e.* almost no change in the gold nanostructure during the oxidative calcination in air at 400 °C or less.[21]

The catalytic performance of the Au/FeO$_x$ catalysts was evaluated for low-temperature CO oxidation. The transient profiles in Fig. 6a reveal the higher activity of Au on Fe_O, compared to Au on Fe_OH (T_{90} = 18 °C *vs.* 63 °C) for the DP samples. In contrast, for the CD synthesis, the Au/Fe_OH was superior to CD_Au/Fe_O (T_{90} = 24 °C *vs.* 56 °C). At a constant temperature of 30 °C (Fig. 6b), the final CO conversions after 10 h on stream were around 38%, 70%, 80% and 40% for samples

Table 2 EXAFS fitting results (R: distance; CN: coordination number) of gold catalysts

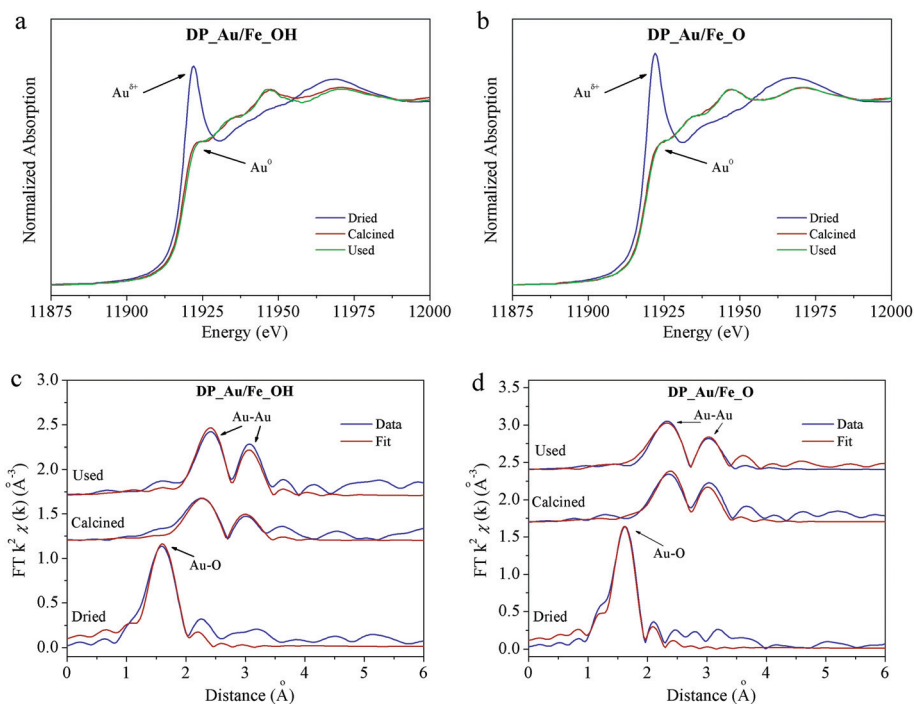|	Au–O		Au–Au	
Sample	R (Å)	CN	R (Å)	CN
Au foil	—	—	2.86 ± 0.00	12
DP_Au/Fe_OH (dried)	2.00 ± 0.02	2.5 ± 0.4	—	—
DP_Au/Fe_O (dried)	2.00 ± 0.00	2.9 ± 0.2	—	—
CD_Au/Fe_OH (dried)	—	—	2.84 ± 0.01	11.1 ± 1.4
CD_Au/Fe_O (dried)	—	—	2.83 ± 0.01	10.4 ± 2.2
DP_Au/Fe_OH (calcined)	—	—	2.84 ± 0.02	9.9 ± 2.1
DP_Au/Fe_O (calcined)	—	—	2.84 ± 0.01	9.8 ± 1.5
DP_Au/Fe_OH (used)	—	—	2.87 ± 0.01	10.1 ± 1.6
DP_Au/Fe_O (used)	—	—	2.84 ± 0.01	10.5 ± 1.5

DP_Au/Fe_OH, DP_Au/Fe_O, CD_Au/Fe_OH and CD_Au/Fe_O, respectively. This deactivation can be ascribed as the carbonate accumulation. Thus, the reactivity of different gold catalysts follows the sequence: DP_Au/Fe_O ≈ CD_Au/Fe_OH > DP_Au/Fe_OH ≈ CD_Au/Fe_O. The activities of the DP_Au/Fe_O and CD_Au/Fe_OH catalysts described here are comparable to those of the commonly coprecipitated gold-iron oxide catalysts, showing even higher gold loadings of ~5 wt%.[7]

Gold sizes in the used DP catalysts were investigated by TEM/HRTEM. Fig. 2 shows that the particles sizes did not change and were around 2 nm before and after the CO oxidation reaction. The related XANES (Fig. 4a and 4b) and EXAFS (Fig. 4c and 4d) spectra give additional evidence on the metallic nature of the nanoparticles. Similar observations with respect to particles size hold for the CD catalysts: the TEM/HRTEM images of the CD catalysts confirm that gold particle

sizes on both Fe_OH and Fe_O supports are constant at ca. 2 nm for dried, calcined and used samples (Fig. 3). It reveals that in CD catalysts the interaction between gold and the iron oxide support does not have a significant influence. The major structure is formed by isolated Au nanoparticles randomly dispersed on the Fe_OH or Fe_O surface, which can be confirmed by the related XAFS results on dried samples (Table 2 and Fig. 5) and very similar to the gold-silica system.[22]

Therefore, CD_Au/Fe_OH and CD_Au/Fe_O can be regarded as reference catalysts for the analysis of the support effect, i.e. ~2 nm Au on hydroxylated (Fe_OH) and dehydrated (Fe_O). Very interestingly, an inverse order of catalytic activity can be clearly seen from the related experimental data between DP (Au/Fe_OH < Au/Fe_O) and CD (Au/Fe_OH > Au/Fe_O). Recently, it has been reported that the surface hydroxyl groups of the support can enhance the activity of supported gold catalyst for CO oxidation.[23–27] For CD-prepared catalysts, it seems that the surface hydroxyl effect plays a dominant role in determining the activity, such that hydroxylated Au/Fe_OH is considerably more active than Au/Fe_O. However, it has an inverse effect for DP-prepared catalysts. This suggests that other factors should be more significant than the surface hydroxyl effect in controlling the reactivity of gold-iron oxide catalysts prepared by the DP method. Because the development of the gold particles follows a much more complex pathway in DP, this is not highly surprising.

First, we focused on the investigation of structural changes of the gold species. Fig. 7 exhibits the in situ XANES results of both DP_Au/Fe_OH and DP_Au/Fe_O. The corresponding fraction of oxidized/reduced gold was calculated by the linear com-

Fig. 4 XANES profiles (a,b) and EXAFS R space fittings (c,d) of Au/FeO_x samples: (a,c) DP_Au/Fe_OH; (b,d) DP_Au/Fe_O.
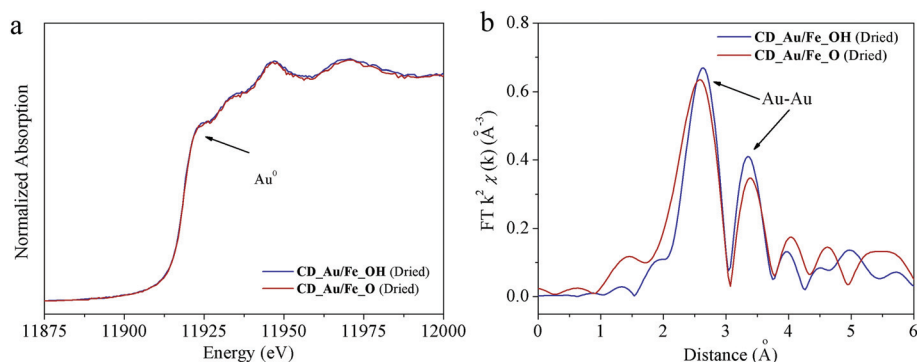
Fig. 5 XANES profiles (a) and EXAFS R space spectra (b) of Au/FeO$_x$ samples (dried CD_Au/Fe_OH and dried CD_Au/Fe_O).
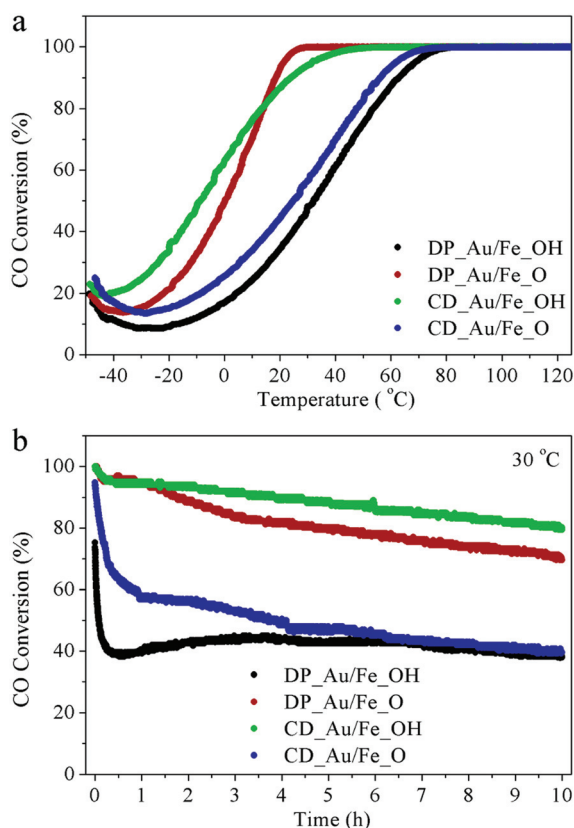

Fig. 6 CO conversions of Au/FeO$_x$ samples measured under (a) transient conditions and (b) at a constant temperature of 30 °C (1%CO/20% O$_2$/79%N$_2$, 80 000 mL h^{-1} g$_{cat}$$^{-1}$).
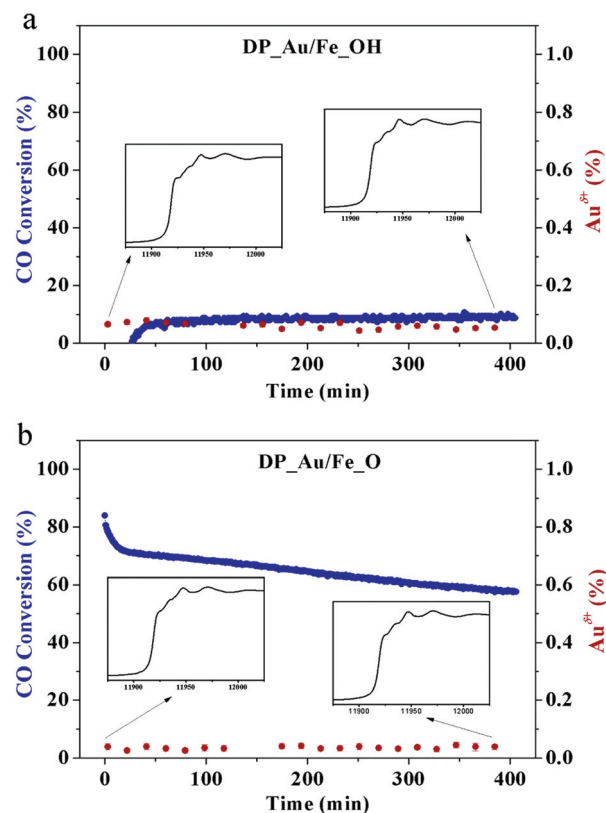

Fig. 7 CO conversions (blue) and Au oxidation states (red) of (a) DP_Au/Fe_OH and (b) DP_Au/Fe_O as function of reaction time (1%CO/ 16%O$_2$/83%He, 20 mL min^{-1}, 25 mg, at 25 °C). Insets are the corresponding XANES spectra taken at the start and end points.

bination method,[28] and the CO conversion was simultaneously monitored by mass spectroscopy. Although the starting Au nanostructures were nearly the same (∼2 nm metallic particles), the CO oxidation activity of gold on the oxide support was considerably higher than that on the hydroxylated support (CO conversion at the end of measurement: 58% *vs.* 10%), which is in good agreement with Fig. 6b. However, the oxidation states of Au were dominantly metallic (Au^0), and the ionic (Au$^{\delta+}$) contributions were below 10% in both samples. In addition, the EXAFS fitting results (Table 2 and Fig. 4) further

prove the predominance of reduced gold nanoparticles in the calcined (before reaction) and used (after reaction) DP catalysts. This demonstrates that the oxidation state is not the dominant factor governing the activity of gold-iron oxide catalysts obtained *via* the DP route.

Another factor which could lead to different catalytic activities of the different DP catalysts could be the transformation of the isolated Au atoms or small clusters (Fig. 2a and 2b) into the Au particles (Fig. 2c and 2d), which takes place during the air-calcination. In order to reveal possible differences, hydro-
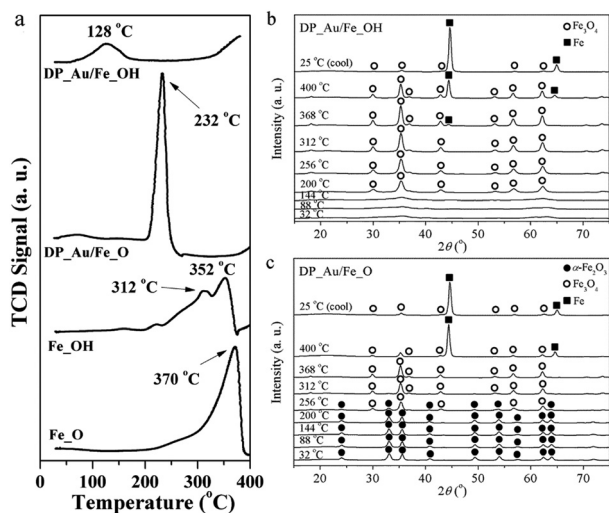
Fig. 8 H_2-TPR profiles (a) and XRD patterns (b,c) under the *in situ* conditions of TPR test: (b) DP_Au/Fe_OH; (c) DP_Au/Fe_O.

Table 3 Hydrogen consumption (H_2-consump.) of gold catalysts

Sample	Reduction peak (°C)	Experimental H_2-consump. (µmol g^{-1})	Theoretical H_2-consump.^{a} (µmol g^{-1})
DP_Au/Fe_OH	128	437	1300
DP_Au/Fe_O	67, 232	1444	1510
CD_Au/Fe_OH	188, 340	235	1300
CD_Au/Fe_O	257	1042	1510

^{a} Calculated according to Fe_OH → Fe_3O_4 or Fe_2O_3 → Fe_3O_4.

gen temperature-programmed reduction (H_2-TPR) was applied to investigate the interaction between metal (Au) and the supports of Fe_OH or Fe_O (Fig. 8 and Table 3). Fig. 8a displays the results: for the pure iron-based support, the main reduction peaks are located between 300 and 400 °C, due to the reduction of α-Fe_2O_3 (hematite) → Fe_3O_4 (magnetite). The introduction of gold led to a decrease in this temperature to about 128 and 232 °C, indicating a pronounced Au–O–Fe interaction.[27] Fig. 8b and 8c show the XRD patterns obtained under *in situ* conditions, similar to the TPR conditions. For DP_Au/ Fe_OH, the starting amorphous hydrated iron oxide was reduced and started to crystallize to Fe_3O_4 at *ca.* 200 °C, and was further reduced to Fe metal above 368 °C (Fig. 8b). For DP_Au/Fe_O, the transformation of the iron oxide from α-Fe_2O_3 → Fe_3O_4 occurs at temperatures above 200 °C, at the final point of the experiment there aremetallic Fe and traces of Fe_3O_4 at 400 °C (Fig. 8c).

For the DP_Au/Fe_O catalyst, there is an intense reduction peak centered at 232 °C. The H_2 consumption related to this reduction peak is 1444 µmol g^{-1}, which is very close to the theoretical value (1510 µmol g^{-1}, Table 3), indicating the full reduction of most of the α-Fe_2O_3 to Fe_3O_4. However, for the DP_Au/Fe_OH, a broad reduction peak centered at 128 °C with a low H_2 consumption value of 437 µmol g^{-1} is observed. The

theoretical value of H_2 consumption related to a full transformation of Fe_OH → Fe_3O_4 is 1300 µmol g^{-1}, which is considerably higher than that of the reduction peak centered at 128 °C for DP_Au/Fe_OH. Therefore, only part of the Fe_OH was reduced to Fe_3O_4 at a temperature of 200 °C (the end of the broad peak), in agreement with the *in situ* XRD pattern at 200 °C, which covers both Fe_3O_4 and some amorphous phases, as shown in Fig. 8b. The TPR results confirm a more effective interaction[20,27] of gold species with iron oxide than with hydroxylated amorphous iron oxide, which explains why the gold on the dehydrated support (Fe_O) is significantly more active than the gold on the hydroxylated support (Fe_OH). It also suggests that the presence of the hydroxylated support prevents the creation of active Au sites during the crystallization of both gold and the iron-oxide support.

On the other hand, for the CD catalysts, the 2 nm Au nanoparticles are already formed before calcination, and the overall interaction between gold and iron-oxide support is less effective than for the DP samples (refer to the lower reduction peak-area for CD_Au/Fe_O in Fig. 9a, and the less hydrogen consumption in Table 3). Based on the related *in situ* XRD results, the phase transformations of iron-oxide support in CD samples (Fig. 9b and 9c) were very similar to those synthesized by DP (Fig. 8b and 8c). Here, the hydroxylated surface is the dominant factor on tuning the Au dispersion/stabilization, and thus the hydroxylated catalyst (CD_Au/Fe_OH) was more active than the dehydrated sample (CD_Au/Fe_O). However, the surface hydroxyl groups may also have an effect because this type of support brings the extra activity enhancement for the gold catalyst systems.[23–27]

From the results described, it can be concluded that the preparation method (DP or CD), the mechanism of formation of the gold particle (locally generated or externally introduced) are crucial in determining the gold reactivity. The deposition-precipitation, or local generation, only benefits from the dehydrated support (Fe_O), while the colloidal-deposition is
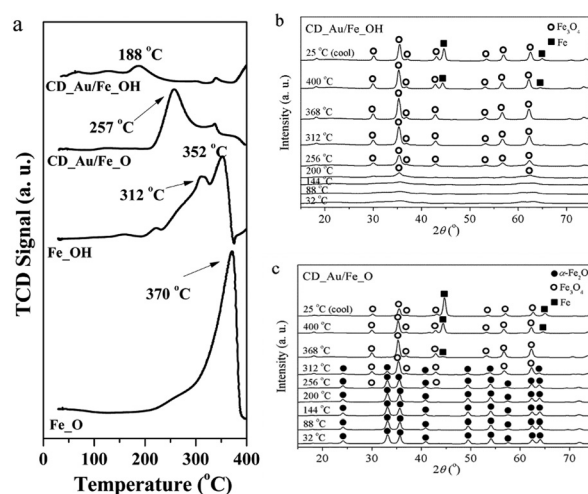

Fig. 9 H_2-TPR profiles (a) and XRD patterns (b,c) under the *in situ* conditions of the TPR test: (b) CD_Au/Fe_OH; (c) CD_Au/Fe_O.

better suited for the hydroxylated support (Fe_OH). For the DP route, the gold particles and their interaction with the support develop during the thermal treatment. Here, it is clear that the more strongly interacting gold species lead to more active catalysts. In the case of the colloidal deposition, the beneficial effect of the hydroxyl groups on the catalyst surface dominates the performance, and thus the gold on the Fe_OH is the more active system for this synthetic pathway.

4. Conclusion

In summary, we have prepared active gold-iron oxide catalysts with uniform size of ~2 nm for gold nanoparticles by both deposition-precipitation and colloidal-deposition methods, and further investigated the main factors in governing the catalytic activity of Au. An inverse order of catalytic activity was found between deposition-precipitation (Au/Fe_OH < Au/Fe_O) and colloidal deposition (Au/Fe_OH > Au/Fe_O) systems. Higher levels of effectiveness of interaction between gold and the oxide support is suggested to account for the superiority of the oxide support (Fe_O) in the deposition-precipitation system, while the surface hydroxyls induce the high reactivity of gold on the hydrated iron oxide support (Fe_OH) for the colloidal-precipitation approach. Thus, the mechanism of formation of the gold species, which is directly related to the synthesis strategy, is a key factor that contributes to the activity of iron oxide supported gold catalysts, in addition to structural effects.

Acknowledgements

References

1 M. Haruta, S. Tsubota, T. Kobayashi, H. Kageyama, M. J. Genet and B. Delmon, *J. Catal.*, 1993, **144**, 175–192.

2 G. C. Bond and D. T. Thompson, *Gold Bull.*, 2000, **33**, 41–50.

3 A. S. K. Hashmi and G. J. Hutchings, *Angew. Chem., Int. Ed.*, 2006, **45**, 7896–7936.

4 A. A. Herzing, C. J. Kiely, A. F. Carley, P. Landon and G. J. Hutchings, *Science*, 2008, **321**, 1331–1335.

5 Y. Liu, C.-J. Jia, J. Yamasaki, O. Terasaki and F. Schuth, *Angew. Chem., Int. Ed.*, 2010, **49**, 5771–5775.

6 J. Guzman and B. C. Gate, *J. Am. Chem. Soc.*, 2004, **126**, 2672–2673.

7 G. J. Hutchings, M. S. Hall, A. F. Carley, P. Landon, B. E. Solsona, C. J. Kiely, A. Herzing, M. Makkee, J. A. Moulijn, A. Overweg, J. C. Fierro-Gonzalez, J. Guzman and B. C. Gates, *J. Catal.*, 2006, **242**, 71–81.

8 N. Weiher, E. Bus, L. Delannoy, C. Louis, D. E. Ramaker, J. T. Miller and J. A. van Bokhoven, *J. Catal.*, 2006, **240**, 100–107.

9 M. M. Schubert, S. Hackenberg, A. C. van Veen, M. Muhler, V. Plzak and R. J. Behm, *J. Catal.*, 2001, **197**, 113–122.

10 M. Kotobuki, R. Leppelt, D. A. Hansgen, D. Widmann and R. J. Behm, *J. Catal.*, 2009, **264**, 67–76.

11 S. Carrettin, P. Concepción, A. Corma, J. M. Lopez Nieto and V. F. Puntes, *Angew. Chem., Int. Ed.*, 2004, **43**, 2538–2540.

12 S. Carrettin, Y. Hao, V. Aguilar-Guerrero, B. C. Gates, S. Trasobares, J. J. Calvino and A. Corma, *Chem. – Eur. J.*, 2007, **13**, 7771–7779.

13 M. Comotti, W. C. Li, B. Spliethoff and F. Schuth, *J. Am. Chem. Soc.*, 2006, **128**, 917–924.

14 C.-J. Jia, Y. Liu, H. Bongard and F. Schuth, *J. Am. Chem. Soc.*, 2010, **132**, 1520–1522.

15 X. Y. Liu, M. H. Liu, Y. C. Luo, C. Y. Mou, S. D. Lin, H. Cheng, J. M. Chen, J. F. Lee and T. S. Lin, *J. Am. Chem. Soc.*, 2012, **134**, 10251–10258; M. Haruta, S. Tsubota, T. Kobayashi, H. Kageyama, M. J. Genet and B. Delmon, *J. Catal.*, 1993, **144**, 175–192.

16 N. Ta, J. Y. Liu, S. Chenna, P. A. Crazier, Y. Li, A. L. Chen and W. J. Shen, *J. Am. Chem. Soc.*, 2012, **134**, 20585–20588.

17 L. Li, A. Q. Wang, B. T. Qiao, J. Lin, Y. Q. Huang, X. D. Wang and T. Zhang, *J. Catal.*, 2013, **229**, 90–100.

18 R. Zanella, S. Giorgio, C. Shin, C. R. Henry and C. Louis, *J. Catal.*, 2004, **222**, 357–367.

19 X. Wang, J. A. Rodriguez, J. C. Hanson, M. Pérez and J. Evans, *J. Chem. Phys.*, 2005, **123**, 221101.

20 W. Deng, A. I. Frenkel, R. Si and M. Flytzani-Stephanopoulos, *J. Phys. Chem. C*, 2008, **112**, 12834–12840.

21 L. F. Allard, A. Borisevich, W. Deng, R. Si, M. Flytzani-Stephanopoulos and S. H. Overbury, *J. Electron Micro.*, 2009, **58**, 199–212.

22 M. T. Bore, H. N. Pham, E. E. Switzer, T. L. Ward, A. Fukuoka and A. K. Datye, *J. Phys. Chem. B*, 2005, **109**, 2873–2880.

23 M. Date and M. Haruta, *J. Catal.*, 2001, **201**, 221–224.

24 G. M. Veith, A. R. Lupini, S. J. Pennycook and N. J. Dudney, *ChemCatChem*, 2010, **2**, 281–286.

25 J. A. Singh, S. H. Overbury, N. J. Dudney, M. J. Li and G. M. Veith, *ACS Catal.*, 2012, **2**, 1138–1146.

26 J. Lin, B. T. Qiao, L. Lin, H. L. Guan, C. Y. Ruan, A. Q. Wang, W. S. Zhang, X. D. Wang and T. Zhang, *J. Catal.*, 2014, **319**, 142–149.

27 W. Deng, C. Carpenter, N. Yi and M. Flytzani-Stephanopoulos, *Top. Catal.*, 2007, **44**, 199–208.

28 A. Piovano, G. Agostini, A. I. Frenkel, T. Bertier, C. Prestipino, M. Ceretti, W. Paulus and C. Lamberti, *J. Phys. Chem. C*, 2011, **115**, 1311–1322.